SAR imaging and hydrodynamic analysis of ocean bottom topographic waves

Quanan Zheng,[1] Li Li,[2] Xiaogang Guo,[2] Yong Ge,[2] Dayong Zhu,[3] and Chunyan Li[4]

Received 15 March 2006; revised 16 May 2006; accepted 12 June 2006; published XX Month 2006.

[1] The satellite synthetic aperture radar (SAR) images display wave-like patterns of the ocean bottom topographic features at the south outlet of Taiwan Strait (TS). Field measurements indicate that the most TS water body is vertically stratified. However, SAR imaging models available were developed for homogeneous waters. Hence explaining SAR imaging mechanisms of bottom features in a stratified ocean is beyond the scope of those models. In order to explore these mechanisms and to determine the quantitative relations between the SAR imagery and the bottom features, a two-dimensional, three-layer ocean model with sinusoidal bottom topographic features is developed. Analytical solutions and inferences of the momentum equations of the ocean model lead to the following conditions. (1) In the lower layer, the topography-induced waves (topographic waves hereafter) exist in the form of stationary waves, which satisfy a lower boundary resonance condition $\sigma = kC_0$, here σ is an angular frequency of the stationary waves, k is a wavenumber of bottom topographic corrugation, and C_0 is a background current speed. (2) As internal waves, the topographic waves may propagate vertically to the upper layer with an unchanged wavenumber k, if a frequency relation $N_3 < \sigma < N_2$ is satisfied, here N_2 and N_3 are the Brunt-Wäisälä frequencies of middle layer and upper layer, respectively. (3) The topographic waves are extremely amplified if an upper layer resonance condition is satisfied. The SAR image of topographic waves is derived on the basis of current-modulated small wave spectra. The results indicate that the topographic waves on SAR images have the same wavelength of bottom topographic corrugation, and the imagery brightness peaks are either inphase or antiphase with respect to the topographic corrugation, depending on a sign of a coupling factor. These theoretical predictions are verified by field observations. The results of this study provide a physical basis for quantitative interpretation of SAR images of bottom topographic waves in the stratified ocean.

Citation: Zheng, Q., L. Li, X. Guo, Y. Ge, D. Zhu, and C. Li (2006), SAR imaging and hydrodynamic analysis of ocean bottom topographic waves, *J. Geophys. Res.*, *111*, XXXXXX, doi:10.1029/2006JC003586.

1. Introduction

[2] Seawater is a high conductivity dielectric medium. Based on the principles of electromagnetic wave propagation, microwave pulses, that radar uses to detect the targets on the earth surface, are capable of penetrating only into a thin layer of seawater with a maximum depth on the order of centimeters. The radar is thus unable to detect the ocean bottom topographic features and underwater objects directly. But, previous investigators have shown since the launch of SEASAT satellite in 1978, that the ocean bottom topographic features, such as tidal flats, submarine sand waves, banks, and shoals, still show up on the SAR images [*Fu and Holt*, 1982; *Lodge*, 1983; *Alpers and Hennings*, 1984; *Shuchman et al.*, 1985; *Apel*, 1987; *Hsu et al.*, 1997; *Alpers et al.*, 2004].

[3] Owing to high spatial resolution, SAR images are able to reveal many details of ocean bottom topographic features, which cannot be found in existing navigation charts. Thus previous investigators suggested using SAR images for ocean bottom topographic mapping [*Hsu et al.*, 1997; *Vogelzang*, 1997; *Alpers et al.*, 2004]. However, this resource cannot practically be used for operational or engineering mapping, unless dynamic links between ocean bottom topographic features and SAR imagery features, including imaging mechanisms and quantitative relationships between the two, are clarified, and accurate inverse methods are established. Hence previous investigators have dedicated continuous efforts to answer this 'what-is-what' question. *Alpers and Hennings* [1984] suggested a radar imaging mechanism of underwater bottom topography,

[1]Department of Atmospheric and Oceanic Science, University of Maryland, College Park, Maryland, USA.
[2]Third Institute of Oceanography, State Oceanic Administration, Xiamen, China.
[3]Department of Oceanography, Xiamen University, Xiamen, China.
[4]Coastal Studies Institute, Department of Oceanography and Coastal Sciences, Louisiana State University, Baton Rouge, Louisiana, USA.

0148-0227/06/2006JC003586$09.00

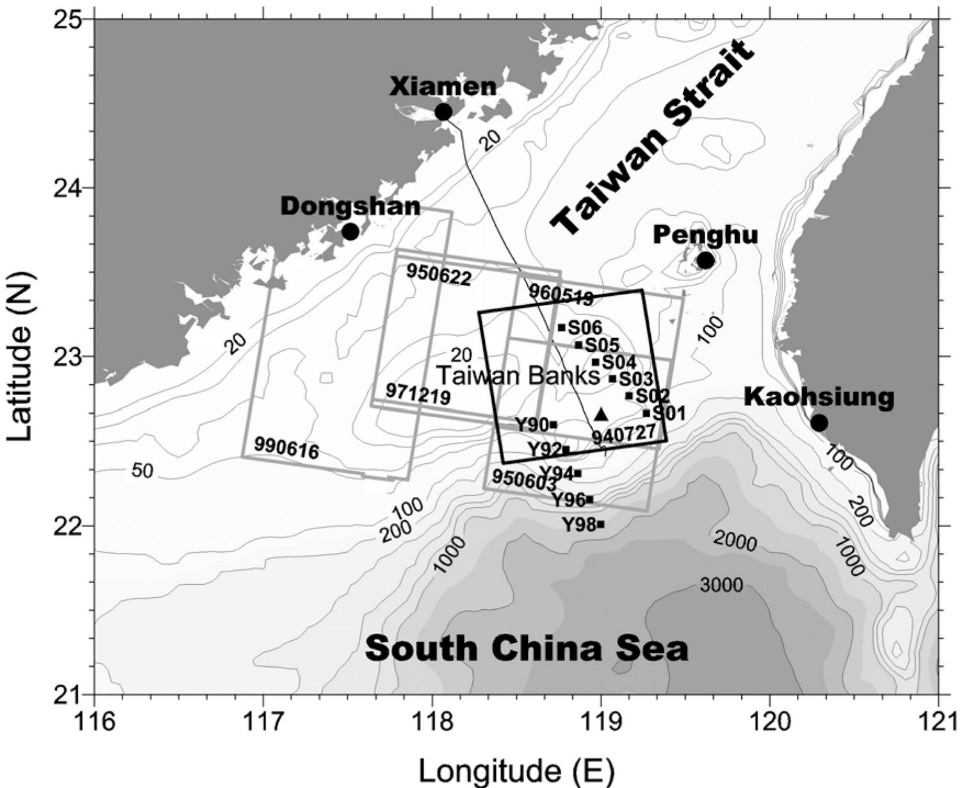

Figure 1. A map of study area with isobaths in meters. Boxes with codes show the ground coverage of SAR images. Triangle in Box 940727 is the location where 3-day anchored tidal measurements were taken. The thin line extending from Xiamen all the way to Box 950603 presents the ship track for high resolution bathymetric measurements using an shipboard ADCP. CTD stations of two transects for cruises of August–September 1994 are also marked.

which is a model relating the topography with surface waves via tidal current modulation. Later, their model was further developed to include the effects of advection [*Vogelzang*, 1989; *Hennings*, 1990] and the effects of the sand wave profiles [*van der Kooij et al.*, 1995]. *Vogelzang* [1997] used the continuity equations to describe modulation of sand waves to the tidal current. *Shuchman et al.* [1985] developed a hydrodynamic and electromagnetic numerical model to investigate SAR imaging conditions of ocean bottom topography.

[4] Most ocean radar imaging models available to date focus on the modulation of variable current to the surface waves. While the underlying ocean is treated as homogeneous, namely the ocean is unstratified and with no-shear of velocity. In the most cases, however, the real ocean can be vertically stratified even in shallow water. *Donato et al.* [1997] carried out intensive air-borne radar imaging flights over ocean bottom sand waves on the continental shelf east of Cape Hatteras, where the water is only 37 m deep, but strongly stratified. Comparing the radar imagery with concurrent accurate observations of bathymetry, they found that the major features of the sand waves on the radar images, such as the maximum signal intensity and the peak value locations, disagree with theoretical predictions derived from the homogeneous models. Thus they suggested that any radar imaging theory must account for both influences of stratification and topography. As one can see later, that in our case, the ocean bottom topographic features located at underwater 100 m depth at the south Taiwan Strait still show up on the SAR images. For such a water area, it is unreasonable to treat the water as homogeneous vertically. In fact, CTD (conductivity-temperature-depth profiler) measurements shown in Figures 2a–2d clearly demonstrate that the vertical stratification becomes an unavoidable hydrodynamic feature at most stations. Therefore a hydrodynamic model needs to be developed. The solutions of the new model must be able to account for the interaction between different layers and the bottom topography, as well as the modulation of the sea surface waves to the radar pulses.

[5] This study aims to establish a SAR imaging hydrodynamic model, which includes both influences from the stratification and topography. The analytical solutions will be sought, and verified using observational data. The model and solutions will then be used to interpret satellite SAR images of bottom topographic waves. Similar methodology has been used to study coastal lee wave [*Zheng et al.*, 1998, 2004], ocean internal wave [*Zheng et al.*, 2001], and estuary jet [*Zheng et al.*, 2004].

[6] This paper is organized as follows. Next section gives a description of the study area and its hydrodynamic conditions including circulation, tides, depth, hydrography, winds, and high-resolution shipboard ADCP (Acoustic Doppler Current Profiler) water depth profile. Section 3 describes satellite SAR images used for this study with preliminary interpretation and statistical analysis. Section 4

Table 1. CTD Stations Within the Study Area

Station	Location	Depth, m	Casting Time, UTC
C044S01	19°16.05′N 22°40.00′E	81	1159 Sep 3, 1994
C044S02	19°10.03′N 22°46.03′E	63	1057 Sep 3, 1994
C044S03	19°04.11′N 22°52.02′E	37	1003 Sep 3, 1994
C044S04	18°58.09′N 22°58.04′E	25	0906 Sep 3, 1994
C044S05	18°52.01′N 23°04.09′E	26	0801 Sep 3, 1994
C044S06	18°45.98′N 23°10.13′E	31	0651 Sep 3, 1994
Y90	22°36.0′N 118°43.0′E	56	0905 Sep 7, 1994
Y92	22°27.2′N 118°47.6′E	92	1023 Sep 7, 1994
Y94	22°18.6′N 118°51.7′E	140	1135 Sep 7, 1994
Y96	22°09.3′N 118°56.0′E	450	1250 Sep 7, 1994
Y98	22°00.5′N 118°59.8′E	1709	1420 Sep 7, 1994

develops a 2-D, three-layer ocean model and gives details for analytical solutions. In section 5, the solutions and inferences are verified with field observations. Section 6 gives conclusions.

2. Study Area and Hydrodynamic Conditions

2.1. Taiwan Banks

[7] Our study area is located at the southern outlet of the Taiwan Strait covering an area from 22° to 24°N latitude, and from 117° to 120°E longitude, i.e., the Taiwan Banks and its adjacent region as shown in Figure 1. About 80% of the total area is shallower than 100 m, the rest 20% on the southeast corner is a portion of the deep South China Sea basin. Near the continental shelf frontal edge, depths descend sharply from 100 m to 2000 m within a distance less than 50 km.

[8] The Taiwan Banks, located from 22.5° to 23.5°N latitude and from 117.5° to 119.3°E longitudes, is a shoal lying across the southern outlet of TS like a threshold. It is separated from the coasts of mainland China on the western side, and from Taiwan Island by the Penghu Channel on the eastern side. The total area is about 8000 km^2. The average water depth is 30 m. The submarine morphology of Taiwan Banks is featured by two-scale subsystems. The large scale subsystem is composed by tidal sand ridges with relative heights of 10 to 20 m extending as long as tens kilometers roughly in a north-south orientation. The small scale subsystem is composed by a vast distribution of hundreds of sand waves. The orientation of sand waves is nearly perpendicular to tidal sand ridges. Field measurements reveal that the heights of sand waves reach 3 to 15 m, and the widths 350 to 500 m. The sand waves are distributed in groups. In a group, the sand waves run parallel to each other with separations much smaller than their widths [*Cai et al.*, 1992]. Using LANDSAT-5 TM (Thematic Mapper) images, *Li et al.* [2001, 2003] estimated that the sand waves roughly take a west-east orientation with lengths from 0.5 to 5 km, and the wavelengths range from 0.35 to 1.5 km. One can see later, these sand waves show up clearly on the SAR images.

2.2. Circulation Systems

[9] Circulation around Taiwan Banks consists of two major subsystems: the South China Sea Warm Current subsystem, which flows northeastward along the shelf break south of Taiwan Banks [*Guan and Fang*, 2006; *Li et al.*, 2000] and enters the eastern strait through the Penhu

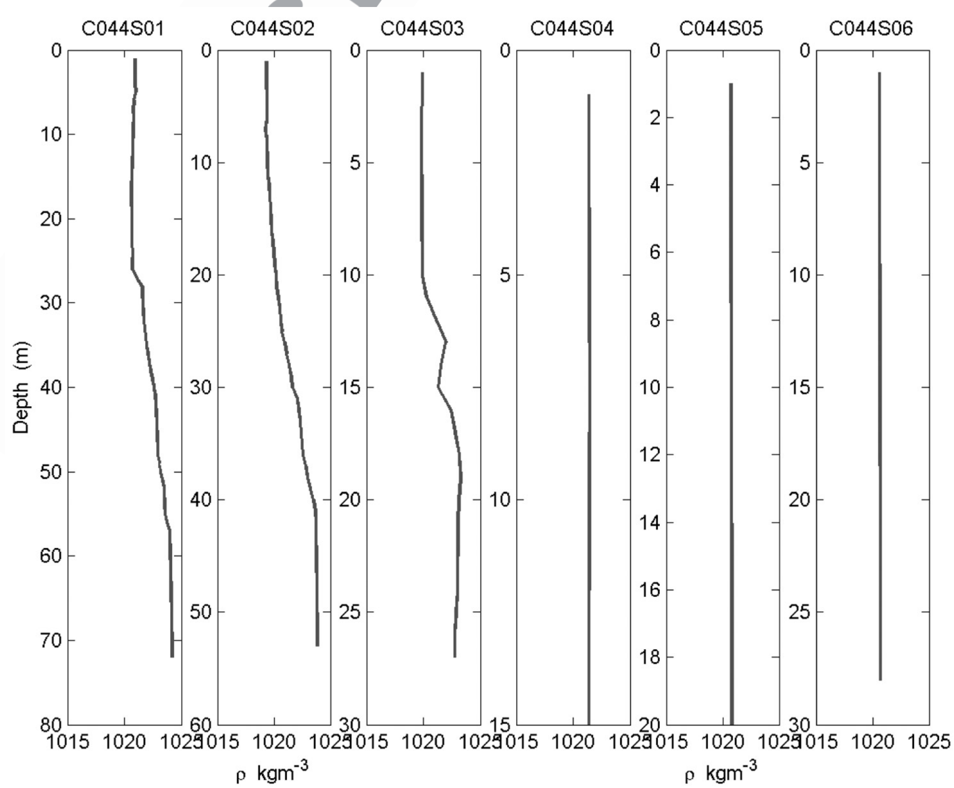

Figure 2a. Vertical profiles of density derived from the CTD data measured by R/V *Ocean Researcher 3* on September 3, 1994.

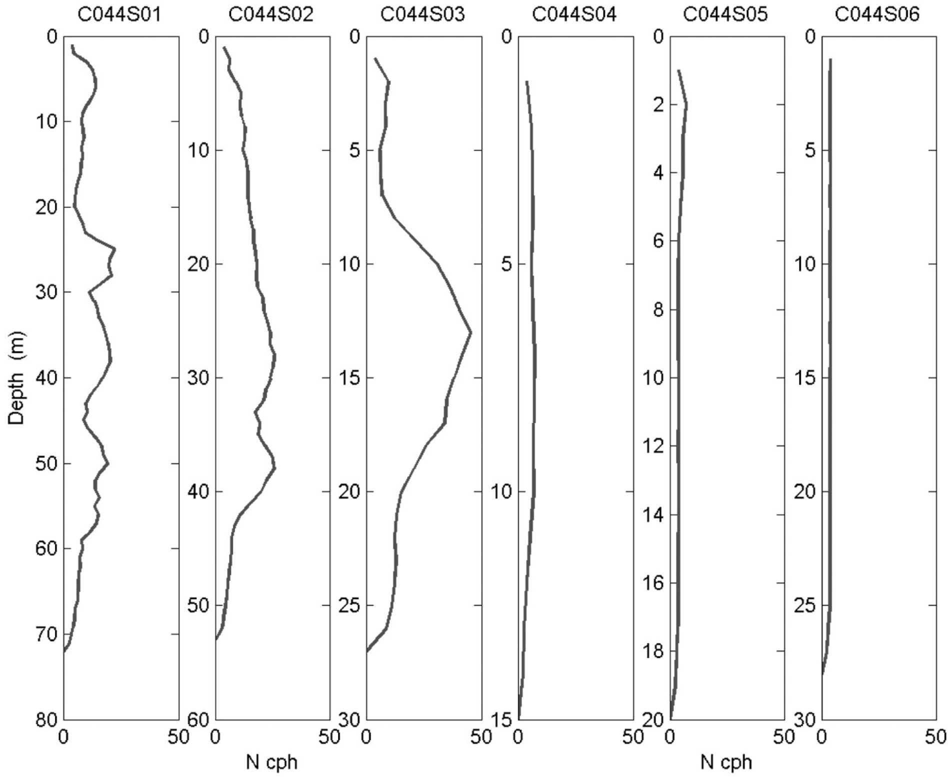

Figure 2b. The corresponding vertical distributions of the Brunt-Wäisälä frequencies of profiles shown in Figure 2a.

Channel flowing northward year-round [*Chuang*, 1986]; and a seasonal varying coastal current subsystem on the west strait modulated by the annual cycle of monsoon wind forcing, which drives a narrow southward jet (so-called Zhejiang-Fujian Coastal Current) along the coasts in winter [*Zheng and Klemas*, 1982] and coastal upwelling with weak horizontal currents and strong upwelling fronts in the channel west to Taiwan Banks [*Li and Li*, 1989; *Li et al.*, 2000]. In any case, these circulation systems have little influence on the study area, which is located at the center of the strait.

2.3. Tides

[10] Unlike the circulation systems, the tidal current plays a key role in the hydrodynamics of the study area. Tides in the TS are dominated by semidiurnal M2 tide with the amplitude as high as 2 m in the middle section. As the Pacific M2 tide propagating into the shallow East China Sea, its amplitude is amplified. A part of this amplified tidal wave propagates southward along the China coast and enters the TS with further amplification. The southward propagating wave and its reflection by the abruptly deepened topography south of the TS lead to the coexistence of a progressive wave in the west and a partial standing wave in the east portion of the strait. The southern branch of the Pacific M2 tide from the Luzon Strait also enters the TS. In comparison to the M2 tide from the north, however, its amplitude is relatively small [*Yin*, 1984].

[11] Tidal currents are weak in the deep water and become stronger over the shallow shelf [*Jan et al.*, 2004, Figure 3b]. Major axes of tidal ellipses are essentially aligned along the strait. In the study area, the northward flood tidal velocity is 3.5 kn and the southward ebb tidal velocity is 2.5 kn [*Hsu et al.*, 1997].

2.4. Vertical Stratification

[12] Hydrographic data used in this study were collected by a joint cruise program between oceanographers from both sides of the TS. The CTD survey of the joint program was conducted in the south TS and adjacent north SCS water. The observations were carried out from August 28 to September 10, 1994 by R/V *Ocean Researcher 3* from Taipei and R/V *Yan Ping* from Xiamen [*Li et al.*, 1998]. There were two transects as marked in Figure 1, just across the Taiwan Banks. The location, water depth, and time of CTD casting at each station are listed in Table 1. The CTD data from these stations were obtained on September 3 and 7, 1994, 36 and 40 days later than the date SAR image 940727 was taken. The data are used to represent approximately the ocean stratification at the SAR imaging time. The vertical profiles of density stratification derived from the CTD data at each station and the Brunt-Wäisälä frequencies, defined as $N^2 = -g\frac{\partial \ln \rho}{\partial z}$, in which g is the gravitational acceleration, and ρ(x, z, t) is the density, corresponding to each density profile are shown in Figures 2a–2d, respectively.

[13] One can see that 8 of 11 stations show strong vertical stratification, and rest three stations (C044S04-06) show weak continuous stratification. These field measurements and derived parameters will serve as a basis for physical ocean model development and dynamic analysis later on.

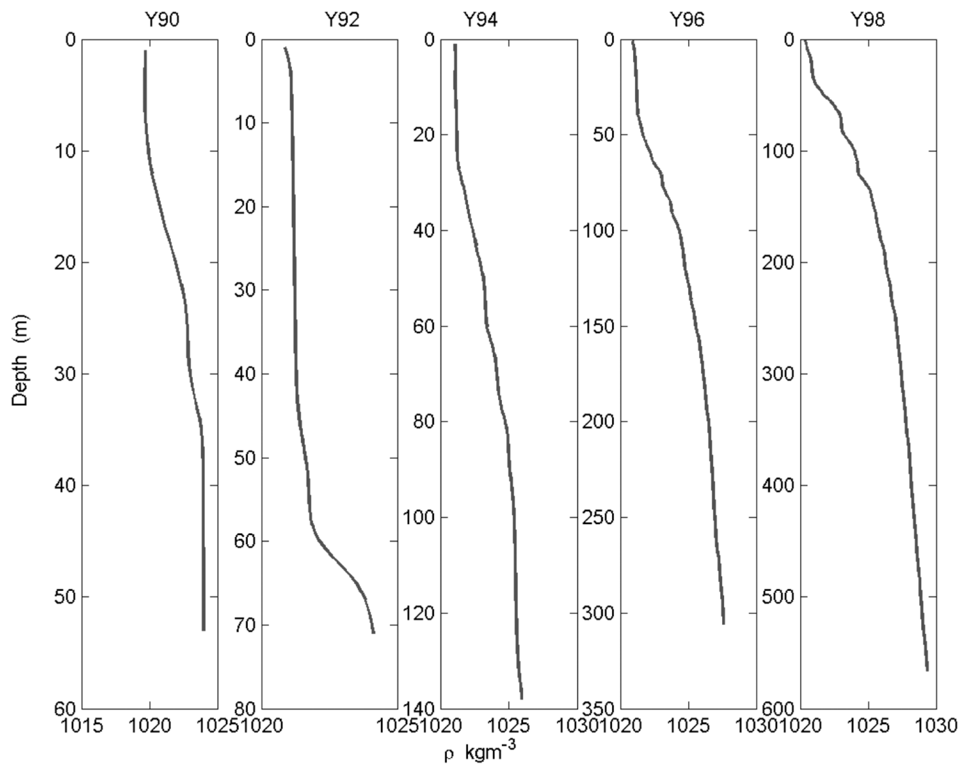

Figure 2c. Vertical profiles of density derived from the CTD data measured by R/V *Yan Ping* on September 7, 1994.

2.5. Sea Surface Winds

[14] Winds over the TS are dominated by the East Asia monsoon, prevailing northeasterly winds in winter and southwesterly winds in summer. The northeast monsoon lasts for nine months a year, beginning in mid-September, reaching a peak phase from December to February, and weakening continuously thereafter till May the next year. The southwest monsoon lasts for only three months from June to August. The northeast monsoon is much stronger than the southwest monsoon. Analyses of satellite scatterometer winds from 1997 to 2001 indicate that the maximum monthly mean wind speeds in the central strait are 8 ms^{-1} in winter, and 3 ms^{-1} in summer, respectively [*Kuo and Ho*, 2004]. This implies that summer is a low wind and low sea state season, which is favorable for SAR imaging of ocean dynamical processes. In fact, most SAR images containing the ocean bottom topographic features collected for this study were taken in summer season.

[15] In our case, there are no simultaneous wind measurements available at the SAR imaging time. In order to estimate the sea state at the imaging time for image 940727, NCEP reanalysis wind field of the day is plotted in Figure 3. One can see that a reasonable estimate of the wind in the study area at the imaging time of 940727 was a southeasterly wind of 3 ms^{-1}, implying a favorable condition for SAR imaging.

2.6. ADCP Water Depth Profiles

[16] High resolution bathymetry was measured by an ADCP on board R/V *Yan Ping* 2 on April 21–22, 2004, along the ship track shown as the thin line from Xiamen to Taiwan Banks in Figure 1 and a bright line shown on image 940727 as an inset of Figure 4. An ADCP sampling time interval of 4 s was used to measure the water depth, that is equivalent to a horizontal distance resolution of about 12 m for an average navigation speed of 6 kn. This horizontal resolution assures the topographic features of interest with a horizontal length scale of 1 km would not be filtered out. The measured depth section is shown in Figure 4. In comparison, the SAR image brightness section along the ship track shown on image 940727 is also given in the figure. One can see that both curves contain multiscale signals, which will be examined later.

3. SAR Images

3.1. Basic Information of SAR Images

[17] A total of six SAR images covering the study area are collected for the analysis. Four images (940727, 960619, 971219, and 990616) are downloaded from the Website http://www.ifm.uni-hamburg.de/ers-sar. The other two (950603 and 950622) are provided by the National Taiwan Ocean University data base (courtesy of C.-R. Ho and M.-K. Hsu). The basic information of the images is listed in Table 2. The ground coverage of each image has been projected on Figure 1. These images were taken by two C band SARs with the same specifications on board ERS-1 and ERS-2 satellites, respectively. The six images cover a time span of six years from 1994 to 1999. Ground coverage of each scene or image is 100 km by 100 km (except 990616, which is a mosaic of two adjacent scenes). The pixel size of raw data of the images is 12.5 m, while the

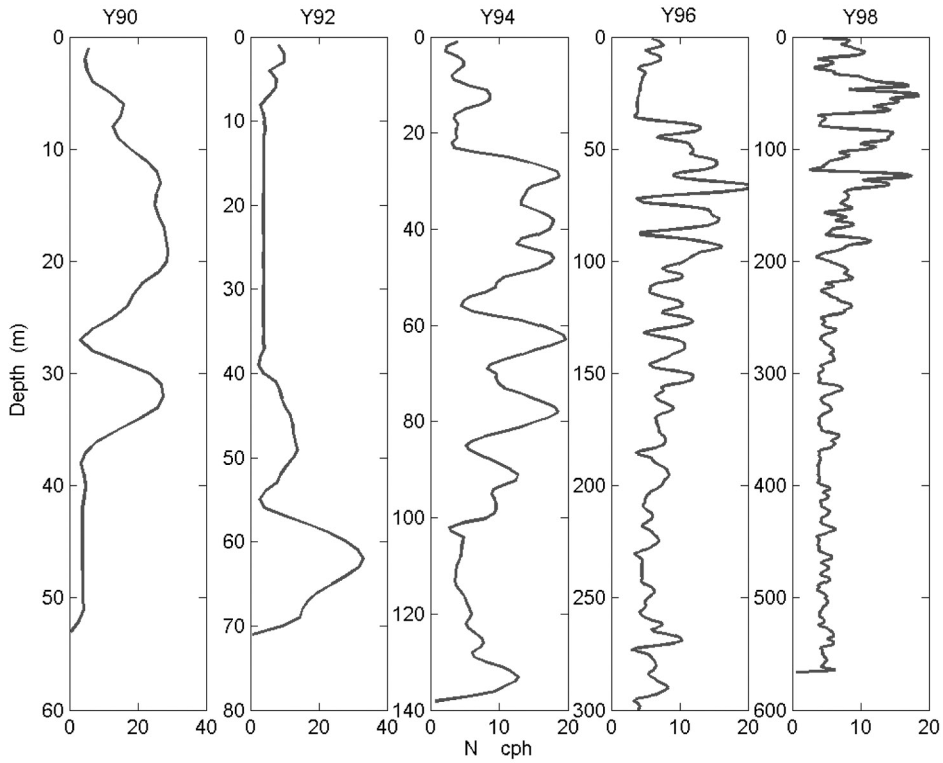

Figure 2d. The corresponding vertical distributions of the Brunt-Wäisälä frequencies of profiles shown in Figure 2c.

ground resolution of all images used for this study has been reduced to 100 m (1000 by 1000 pixels per scene).

[18] Compared to the coastlines and islands on maps and charts, as well as ocean bottom features shown on well-registered LANDSAT TM images, we find that the central positions of the SAR images given in the Website and database are not accurate enough. Therefore we have redetermined these positions according to coastlines and bottom topographic feature on both TM and SAR images. The results are given in Table 2.

[19] Among the six images, image 940727 shown in Figure 5 serves as a main target for this study, because of more imagery information than others. Hundreds of grouped, wave-like, bright-dark patterns on the image show the surface manifestations of bottom topographic features of the eastern Taiwan Banks. CTD data show that the depth for bottom topographic features to show up on the SAR image reaches around 100 m.

3.2. Tidal Phase and Velocity at SAR Imaging Time

[20] The tidal current is considered as a major factor for generating the bottom topographic wave signals on the SAR images. Thus tidal phase is relevant to the characteristics of the SAR images. As described in section 2.3, the amplitude of tidal currents at the study area is about 1.5 ms^{-1}, and the major axis of the prevailing M_2 tide is basically parallel to the NNE-SSW orientation of the Strait. Namely, the topographic waves observed are basically perpendicular to the tidal current axis. In order to determine the tidal phase at the SAR imaging time, continuous tide data are needed. Unfortunately, there are no direct observations available at the study area. Instead, the tide gauge data recorded at two nearby stations, Xiamen (24°27.0′N 118°04.0′E) on the west coast of the TS, and Kaohsiung (22°36.6′N 120°17.5′E) on the east coast, are used to extrapolate the tidal phase at SAR imaging time. The results show (Figure 6) that in 5 of 6 cases (except 950622,) the SAR imaging times fall within a ±1.5 h span during ebb tides from mid to low waters with respect to Xiamen, and during flood tides from low to mid waters with respect to Kaohsiung. Since the local tide lags Kaohsiung for about 1 hour and leads Xiamen for 3 hours, these SAR images were recorded during the first half of local flooding shortly after low tide. On the other hand, image 950622 was recorded during the first half of local ebbing after high tide. This implies that a certain level of tidal current velocity is needed to sustain the existence of hydrodynamic disturbances of topographic waves, although their time of generation cannot be determined directly by SAR observations.

[21] The tidal velocity at the SAR imaging time is not available. Based on 3-day anchored measurements at the topographic wave area marked by a triangle in Figure 1 [*Chen et al.*, 1999] and the results by previous investigators [*Yin*, 1984; *Hsu et al.*, 1997; *Jan et al.*, 2004], a reasonable estimate for the tidal velocity is about 1.5 ms^{-1}.

4. Hydrodynamic Analysis

4.1. Physical Model

[22] Based on the measurements of the vertical stratification and bottom topography, a two-dimensional, three-layer model is developed as shown in Figure 7 using a Cartesian coordinate system. The origin is located at the bottom. The z axis is positive upward. The horizontal axis x is perpen-

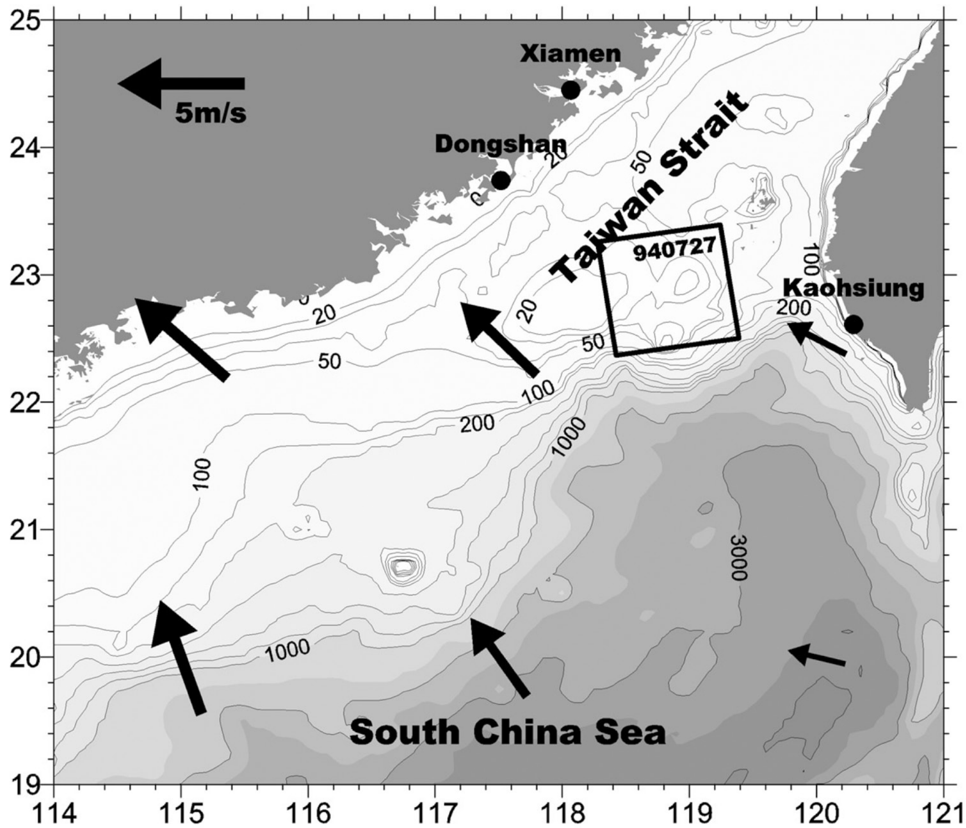

Figure 3. NCEP wind field at the imaging time of SAR image 940727 shown in Figure 5.

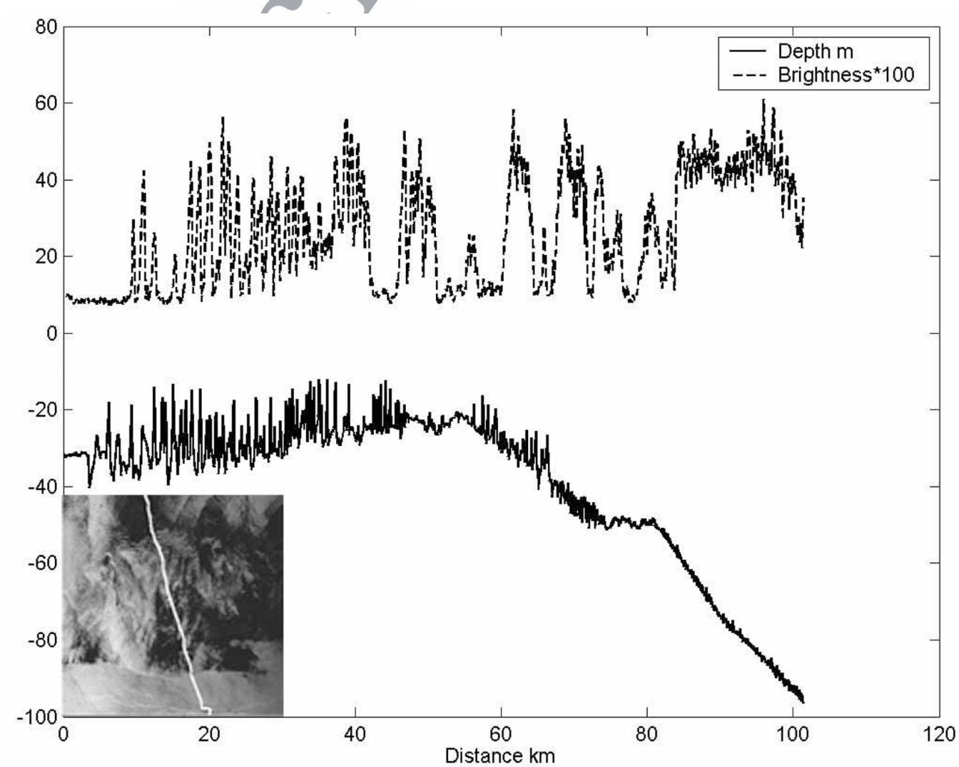

Figure 4. Water depth profile measured by a shipboard ADCP (lower) and corresponding image brightness (upper) along the ship track shown on SAR image 940727 (inset).

Table 2. Basic Information of SAR Images Used for This Study

Code	Satellite	Date and Time, UTC	Orbit	Frame	Central Position (Corrected)
940727	ERS-1	Jul 27, 1994 14:31	15850	441	23°02′N 118°32′E
950603	ERS-1	Jun 3, 1995 2:37	20303	3159	22°36′N 118°52′E
950622	ERS-1	Jun 22, 1995 2:40	20575	3159	23°05′N 118°12′E
960519	ERS-2	May 19, 1996 2:37	05640	3159	22°58′N 118°50′E
971219	ERS-2	Dec 19, 1997 2:40	13928	3141	23°07′N 118°12′E
990616	ERS-2	Jun 16, 1999 2:43	21715	3123–3141	23°08′N 117°30′E

dicular to the axis of bottom topographic corrugation and positive downstream. In other words, the ocean current is a crossing flow with respect to the bottom topographic waves. Assume that the ocean with a depth of D can be into three layers. The lower layer has a thickness of H, the middle layer, $2\Delta H$, and the upper layer, H_3 [$=D - (H + 2\Delta H)$]. The Brunt-Wäisälä frequencies in the three layers are constants N_1, N_2, and N_3, respectively. As the lower rigid boundary of the ocean, the bottom topographic waves constitute a small-amplitude corrugation, sinusoidal in x, i.e., $\eta = (\eta_s/\pi)e^{ikx}$, where η_s ($\ll H$) is the amplitude, and k ($=2\pi/\lambda$, in which λ is the wavelength.) is the wave number. Only the real part is meant in applications. For convenience, we assume that there is no vertical shear in the horizontal velocity in each layer.

4.2. Wave Equations and Solutions

[23] We adopt the methods used in the analysis of the atmospheric gravity wave to our case [*Gossard and Hooke*, 1975]. The fluid is considered to be incompressible. The wave is assumed two-dimensional, and propagates in the xz-plane. The momentum equations are

$$\frac{\partial u}{\partial t} = -\frac{1}{\rho_0}\frac{\partial p}{\partial x}, \tag{1}$$

$$\frac{\partial w}{\partial t} = -\frac{1}{\rho_0}\frac{\partial p}{\partial z} - g\frac{\rho}{\rho_0}, \tag{2}$$

$$\frac{\partial \rho}{\partial t} + w\frac{\partial \rho_0}{\partial z} = 0, \qquad \frac{\partial u}{\partial x} + \frac{\partial w}{\partial z} = 0, \tag{3}$$

where u and w are the horizontal and vertical velocity components, respectively, p is the pressure, and ρ ($=\rho_0 + \varepsilon\rho_1 + \varepsilon^2\rho_2 + \ldots$) is the density. From (2) and (3) we have

$$\frac{\partial^2 w}{\partial t^2} + \frac{1}{\rho_0}\frac{\partial}{\partial t}\left(\frac{\partial p}{\partial z}\right) - \frac{g}{\rho_0}\frac{\partial \rho_0}{\partial z}w = 0. \tag{4}$$

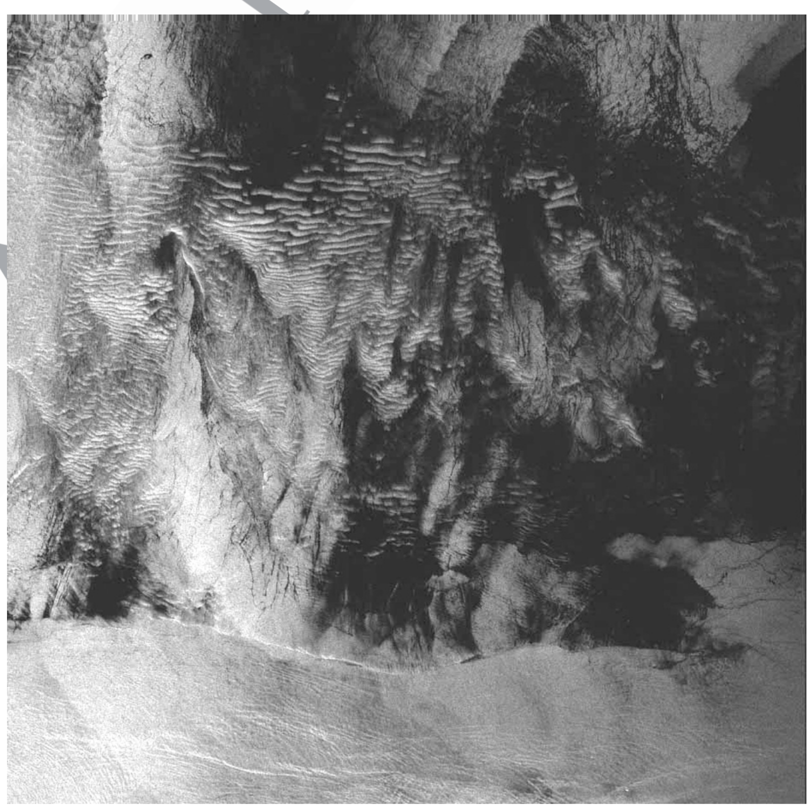

Figure 5. SAR image 940727 of the Taiwan Banks taken by ERS-1 satellite on July 27, 1994, 14:31 UTC. The image is centered at 23°02′N 118°32′E, located at the southern outlet of the Taiwan Strait.

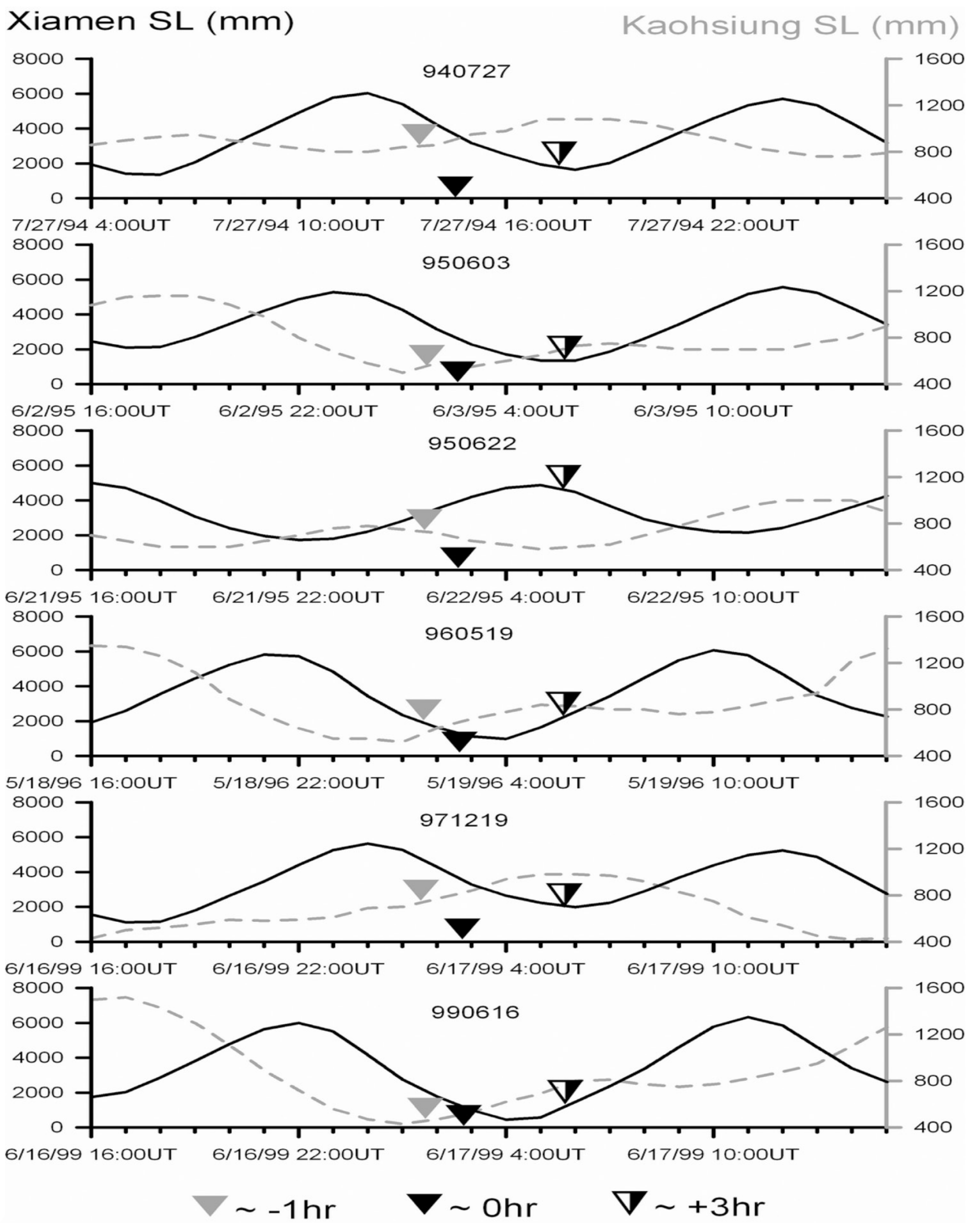

Figure 6. SAR imaging times (dark reverse triangles) and tides at two nearby tide gauges, Xiamen (24°27.0′N 118°04.0′E, dark lines) on the west coast of the Taiwan Strait, and Kaohsiung (22°36.6′N 120°17.5′E, dashed lines) on the east coast. Split reverse triangles and light reverse triangles show the corresponding tidal phases with respect to Xiamen (3-hour lag) and Kaohsiung (1-hour lead), respectively.

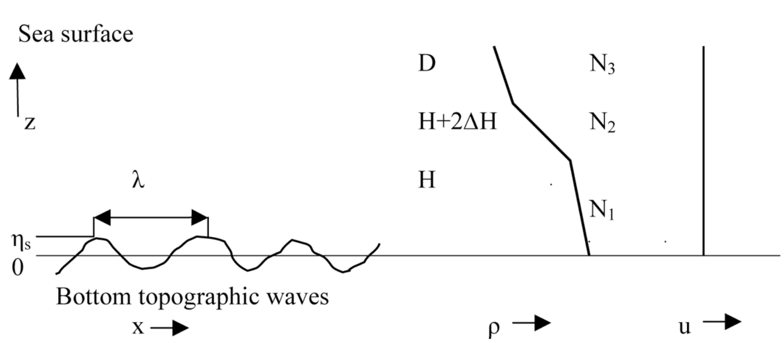

Figure 7. Schematic illustration of a two-dimensional, three-layer model ocean.

From (1) and (3) we have

$$\frac{1}{\rho_0}\frac{\partial^2 p}{\partial x^2} = \frac{\partial}{\partial t}\left(\frac{\partial w}{\partial z}\right). \quad (5)$$

Propose (4) and (5) have solutions of the form

$$(w, p) = (w_z, p_z)\exp i(kx - \sigma t), \quad (6)$$

where σ (=$2\pi/T$, and T is the period of the horizontal component) is the angular frequency. Further eliminating p in (4) yields the wave equation in w_z as

$$\frac{\partial^2 w_z}{\partial z^2} + \frac{1}{\rho_0}\frac{\partial \rho_0}{\partial z}\frac{\partial w_z}{\partial z} + \frac{k^2}{\sigma^2}\left(N^2 - \sigma^2\right)w_z = 0. \quad (7)$$

Here N is defined as in section 2.4. Supposing $\rho_0 = \rho_s e^{-\alpha z}$, in which ρ_s is the density at a reference depth, and α is a constant, and using the variable transformation of the form

$$W_z = \left(\frac{\rho_0}{\rho_s}\right)^{1/2} w_z, \quad (8)$$

Equation (7) becomes

$$\frac{\partial^2 W_z}{\partial z^2} + \left[\frac{k^2}{\sigma^2}\left(N^2 - \sigma^2\right) + \left(\frac{1}{2\rho_0}\frac{\partial \rho_0}{\partial z}\right)^2\right]W_z = 0. \quad (9)$$

If the coefficient of the second term is a constant

$$n^2 = \frac{k^2}{\sigma^2}\left(N^2 - \sigma^2\right) + \left(\frac{1}{2\rho_0}\frac{\partial \rho_0}{\partial z}\right)^2, \quad (10)$$

Equation (9) has plane wave solutions in the form of

$$W_z = A\exp i(kx + nz - \sigma t). \quad (11)$$

Here n is the vertical wave number corresponding to the horizontal wave number k. Equation (10) is the dispersion relation or characteristic equation.

[24] For a three-layer model ocean as shown in the middle of Figure 7, solutions satisfying the kinematic boundary conditions at the interface between two layers, i.e.,

$$\frac{\partial W_i}{\partial z} = \frac{\partial W_{i+1}}{\partial z}, \qquad i = 1, 2 \quad (12)$$

are as follows [*Gossard and Munk*, 1954]

$$W_1 = W_H \frac{\sinh\gamma_1 z + M\cosh\gamma_1 z}{\sinh\gamma_1 H + M\cosh\gamma_1 H}\exp[i(kx - \sigma t)], \quad (13)$$

$$W_2 = W_H \frac{\sinh n_2(z - H) + M_0\cosh n_2(z - H)}{M_0}\exp[i(kx - \sigma t)], \quad (14)$$

$$W_3 = W_H \frac{\sin n_2(2\Delta H) + M_0\cos n_2(2\Delta H)}{M_0} \cdot \exp[-\gamma_3\{z - (H + 2\Delta H)\} + i(kx - \sigma t)], \quad (15)$$

where W_H is the wave amplitude at the depth H, and γ_1, $\gamma_3 = -i(n_1, n_3)$. Applying the dynamic boundary condition (12) at $z = H + 2\Delta H$ yields

$$M_0 = \frac{n_2\cos 2n_2\Delta H + \gamma_3\sin 2n_2\Delta H}{-\gamma_3\cos 2n_2\Delta H + n_2\sin 2n_2\Delta H}. \quad (16)$$

Similarly at $z = H$, we obtain

$$M = \frac{(n_2/M_0)\sinh\gamma_1 H - \gamma_1\cosh\gamma_1 H}{\gamma_1\sinh\gamma_1 H - (n_2/M_0)\cosh\gamma_1 H}. \quad (17)$$

4.3. Stationary Wave Solutions

[25] As shown in Figure 7, the lower boundary of the model ocean is a small-amplitude sinusoidal corrugation. If this boundary is moved with velocity C_0 in the negative x-direction beneath an ocean half-space, from the continuity equation (3) we derive the boundary perturbation of vertical velocity as

$$W(0) = (W_s/\pi)\exp[ik(x + C_0 t)]. \quad (18)$$

This is equivalent to an ocean current with a speed C_0 flowing in the positive x direction across a stationary corrugation and establishing a system of stationary waves [*Gossard and Hooke*, 1975]. Substituting (18) into (13) and letting $H = 0$ yield a stationary solution in the form of

$$W_1(x, z, t) = (W_s/\pi M)(\sinh\gamma_1 z + M\cosh\gamma_1 z)e^{ikx}, \quad (19)$$

if a condition

$$\sigma = kC_0 \quad (20)$$

is satisfied. We call this condition the lower layer resonance condition (LLRC). Similarly, from (14) and (15) we have

$$W_2(x, z) = (W_s/\pi M_0)[\sin n_2(z - H) + M_0\cos n_2(z - H)]e^{ikx}, \quad (21)$$

and

$$W_3(x, z) = (W_s/\pi M_0)[\sin n_2(2\Delta H) + M_0\cos n_2(2\Delta H)] \bullet \exp[-\gamma_3\{z - (H + 2\Delta H)\} + ikx]. \quad (22)$$

[26] Besides the dynamic boundary condition, our case requires a special boundary condition, i.e., W_3 trends toward a small quantity at $z = D$ (sea surface). This requires γ_3 in (15) to be real. In other words, n_3 must be imaginary. Writing $n_3 = in_p$, then $\gamma_3 = n_p$, in which

$$n_3^2 = \frac{k^2}{\sigma^2}\left(N_3^2 - \sigma^2\right) + \left(\frac{1}{2\rho_0}\frac{\partial \rho_0}{\partial z}\right)^2. \quad (23)$$

The condition for γ_3 being real requires

$$N_3 < \sigma, \left|\frac{k^2}{\sigma^2}\left(N_3^2 - \sigma^2\right)\right| > \left(\frac{1}{2\rho_0}\frac{\partial \rho_0}{\partial z}\right)^2. \quad (24)$$

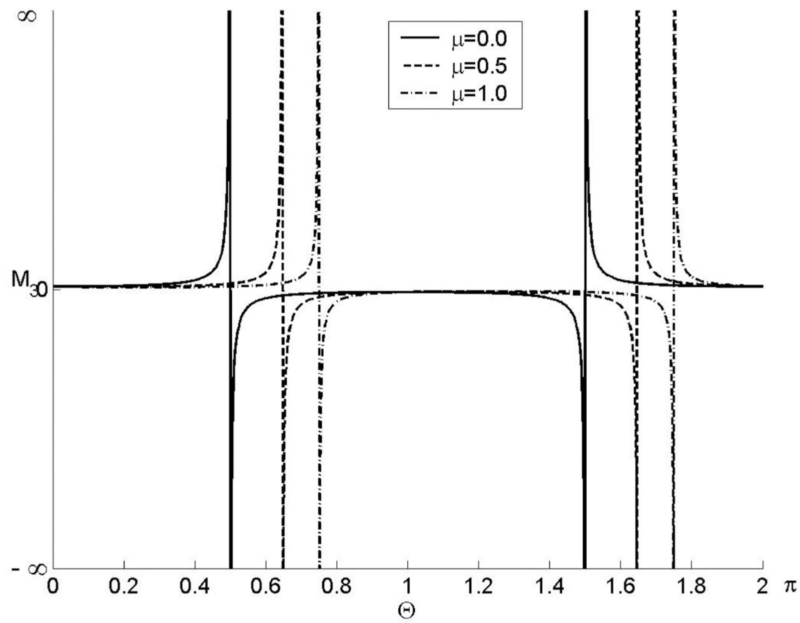

Figure 8. Schematic expressions of the coupling factor M_3 (see the text for parameter definitions).

On the other hand, n_2 is real, implying $N_2 > \sigma$. Therefore the topographic wave propagating vertically in the three-layer model ocean must satisfy a frequency relation

$$N_3 < \sigma < N_2. \qquad (25)$$

[27] We define a coupling factor

$$M_3 = \frac{\sin n_2(2\Delta H) + M_0 \cos n_2(2\Delta H)}{M_0}. \qquad (26)$$

Thus

$$W_3(x,z) = (W_s/\pi)M_3 \exp[-\gamma_3\{z-(H+2\Delta H)\} + ikx].$$

One can see that M_3 can be used as an index for the efficiency of wave momentum transfer from the middle layer to the upper layer. In the case for $\gamma_3 = n_p$, we have

$$M_3 = \frac{n_2}{n_2 \cos n_2(2\Delta H) + n_p \sin n_2(2\Delta H)}. \qquad (27)$$

From equation (27), one can see that the coupling factor M_3 depends on the stratification parameters of the middle and upper layers and the wave parameters of topographic waves. For convenience, (27) may further be simplified as

$$M_3 = \frac{1}{\cos\Theta + \mu \sin\Theta}, \qquad (28)$$

where $\Theta = n_2(2\Delta H)$, implying a phase thickness of the middle layer, and $\mu = n_p/n_2$, implying a relative decay rate in the upper layer, respectively. For further understanding the physical meaning, we rewrite Θ as

$$\Theta = \left[\frac{k^2}{\sigma^2}\left(N_2^2 - \sigma^2\right) + \left(\frac{1}{2\rho_0}\frac{\partial\rho_0}{\partial z}\right)^2\right]^{1/2}(2\Delta H).$$

Assuming the second term in the square bracket is negligibly small in comparison to the first term, we have

$$\Theta = \left[\left(\frac{N_2}{\sigma}\right)^2 - 1\right]^{1/2}\left[2\pi\left(\frac{2\Delta H}{\lambda}\right)\right]. \qquad (29)$$

One can see that Θ is dependent on the frequency ratio and the length scale ratio between those of the middle layer and the topographic wave.

[28] The schematic expressions of (28) are shown in Figure 8, in which μ serves as an adjustable parameter. One can see that the topographic wave may extremely amplified as propagating into the upper layer for a very narrow ranges of Θ.

[29] Now we discuss two special cases.

[30] 1. For $\mu \ll 1$, we have

$$M_3 \approx \sec\Theta. \qquad (30)$$

This implies

$$M_3 \to \infty, \quad for \quad \Theta = \left(m + \frac{1}{2}\right)\pi, \quad m = 0, 1, 2, \ldots \qquad (31)$$

[31] 2. For $\mu \approx 1$, we have

$$M_3 \approx \frac{\sqrt{2}}{2}\sec\left(\Theta - \frac{\pi}{4}\right). \qquad (32)$$

This implies

$$M_3 \to \infty, \quad for \quad \Theta = \left(m + \frac{3}{4}\right)\pi, \quad m = 0, 1, 2, \ldots \qquad (33)$$

We call (31) and (33) the upper layer resonance conditions (ULRC).

[32] From the continuity equation (3) and equation (22), we have the horizontal velocity component in the upper layer

$$u_3(x,z) = \left(n_p/ik\right)(W_s/\pi)M_3 \exp\left[-n_p\{z-(H+2\Delta H)\}+ikx\right]. \tag{34}$$

At the sea surface

$$u_3(x,D) = \left(n_p/k\right)(W_s/\pi)M_3 \exp\left[-n_pH_3+i\left(kx-\frac{\pi}{2}\right)\right]. \tag{35}$$

where $H_3 = D - (H + 2\Delta H)$ is the upper layer thickness. Compared to (19), one can see that the wave keeps the horizontal patterns of the topographic waves, but has a phase shift of $\pi/2$.

4.4. SAR Image of Topographic Waves

[33] In order to extract information about the bottom topographic waves from SAR images, it is necessary to derive a theoretical expression of the topographic wave in a SAR image. In other words, we must determine the quantitative relations between sea surface radar return signals and hydrodynamic parameters of the topographic waves. If a radar receiving system is considered linear, the intensity of radar return signals should linearly depend on a backscatter cross section per unit area defined as [*Plant*, 1990]

$$\sigma_\circ(\theta)_{ij} = 16\pi k_0^4\left|g_{ij}(\theta)\right|^2(0, 2k_0\sin\theta), \tag{36}$$

where θ is the incidence angle, k_0 is the wave number of the radar waves, and Ψ is the two-dimensional (Cartesian) wave number spectral density of the ocean surface wavefield which satisfies the Bragg resonant scatter condition, the incident radiation is in the x-z plane (z being the vertical direction and x, y the horizontal coordinates), the indices ij denote the polarizations of the incident and backscattered radiation, respectively, and $g_{ij}(\theta)$ is the first-order scattering coefficient for given i. For horizontal polarization

$$g_{HH}(\theta) = \frac{(\varepsilon_r-1)\cos^2\theta}{\left[\cos\theta+\left(\varepsilon_r-\sin^2\theta\right)^{1/2}\right]^2}, \tag{37}$$

and for vertical polarization

$$g_{VV}(\theta) = \frac{(\varepsilon_r-1)\left[\varepsilon_r\left(1+\sin^2\theta\right)-\sin^2\theta\right]\cos^2\theta}{\left[\varepsilon_r\cos\theta+\left(\varepsilon_r-\sin^2\theta\right)^{1/2}\right]^2}, \tag{38}$$

where ε_r is the relative dielectric constant of seawater [*Saxton and Lane*, 1952; *Klein and Swift*, 1977].

[34] From (36), one can see that for a satellite radar with a fixed wavelength and a fixed incidence angle, the intensity of radar return signals depends only on the wave number spectral density of the ocean surface wavefield Ψ. Considering the modulation of short ocean surface waves by wave-current interaction, *Yuan* [1997] derived the wave number spectral density of the high frequency ocean surface wavefield in the form of

$$= \begin{cases} m_3^{-1}\left[m\left(\frac{u*}{c}\right)^2 - 4\nu_s K^2\omega^{-1} - S_{\alpha\beta}\frac{\partial U_\beta}{\partial x_\alpha}\omega^{-1}\right]K^{-4} & \text{for gravity-capillary wave band,} \quad (39a) \\ m_4^{-1/2}\left[m\left(\frac{u*}{c}\right)^2 - 4\nu_s K^2\omega^{-1} - S_{\alpha\beta}\frac{\partial U_\beta}{\partial x_\alpha}\omega^{-1}\right]^{1/2}K^{-4} & \text{for capillary wave band,} \quad (39b) \end{cases}$$

where m, m_3, and m_4 are coefficients, u_* is the friction velocity, c is the wave phase speed, ν_s is the viscosity of seawater, ω is the angular frequency of the ocean surface waves, K is the wave number of ocean surface waves, and

$$S_{\alpha\beta}\frac{\partial U_\beta}{\partial x_\alpha} = \left[\frac{\partial u}{\partial x}\cos^2\phi + \left(\frac{\partial u}{\partial y}+\frac{\partial v}{\partial x}\right)\cos\phi\sin\phi + \frac{\partial v}{\partial y}\sin^2\phi\right]/2, \tag{40}$$

where u and v are velocity components, and φ is the wave direction. One can see that the spectral density function consists of three terms, which represent the wind-forcing, the dissipation induced by the viscosity, and modulation induced by a variable current, respectively [*Zheng et al.*, 2001]. In our case, the Taiwan Banks are far away from the coasts and estuaries; therefore it is acceptable to assume that the seawater viscosity and wind field are homogeneous within one scene of SAR image (100 km by 100 km). Thus their contributions to a radar image can be considered as a uniform background, which would not generate any bright or dark patterns. In this case, the current modulation term plays a key role in generating an ocean feature radar image.

[35] The SAR images analyzed in this study were taken by a C band radar, whose the microwave wavelength corresponds to the sea surface gravity-capillary wave band. Thus substituting (39) into (36) yields

$$\sigma_\circ(\theta)_{ij} = 16\pi k_0^4\left|g_{ij}(\theta)\right|^2 m_3^{-1}\left[m\left(\frac{u_*}{c}\right)^2 - 4\nu_s K^2\omega^{-1}\right] \cdot K^{-4} - 16\pi k_0^4\left|g_{ij}(\theta)\right|^2 m_3^{-1}\left[S_{\alpha\beta}\frac{\partial U_\beta}{\partial x_\alpha}\omega^{-1}\right]K^{-4}.$$

As analyzed above, the first term can be considered as a constant. Thus the imagery patterns of the ocean are generated by the second term, i.e.,

$$\sigma_\circ|_{os} = -16\pi k_0^4\left|g_{ij}(\theta)\right|^2 m_3^{-1}\left[S_{\alpha\beta}\frac{\partial U_\beta}{\partial x_\alpha}\omega^{-1}\right]K^{-4}. \tag{41}$$

In the case of ocean bottom topographic waves, the functional form of ocean current velocity at the sea surface has been derived in (35). Substituting (35) into (40) and taking the real part yield

$$S_{\alpha\beta}\frac{\partial U_\beta}{\partial x_\alpha} = \frac{n_p W_s}{2\pi}M_3 e^{-n_p H_3}\cos^2\phi\cos kx. \tag{42}$$

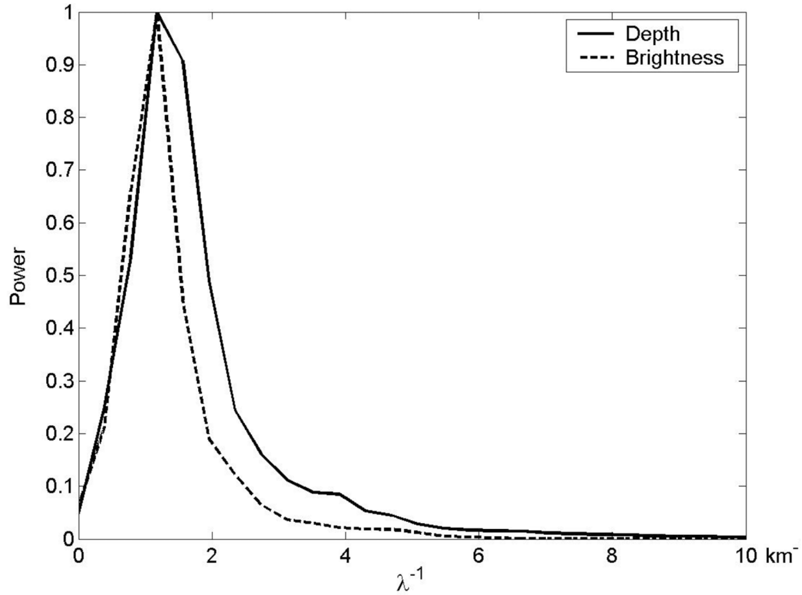

Figure 9. A comparison of wave number spectra (λ^{-1}) of high-pass-filtered ocean bottom corrugation (solid line) to that of corresponding radar return brightness (dashed line).

Substituting (42) into (41) yields an analytical expression of SAR image of bottom topographic waves

$$\sigma_\circ|_{os} = -\left[16\pi k_0^4 |g_{ij}(\theta)|^2\right] \bullet \left[\frac{\cos^2\phi}{2m_3\omega K^4}\right] \bullet \left[\frac{n_p W_s}{\pi} M_3 e^{-n_p H_3}\right] \cos kx. \tag{43}$$

One can see that the bottom topographic waves on the SAR image also appear as the form of a cosinoidal function with the same wave number of the original topographic waves. The amplitude or intensity of radar signal depends on three factors, which are defined by radar wave number and incidence angle, sea surface gravity-capillary wavefield, and ocean vertical stratification as given in the three square brackets in (43), respectively. Moreover, it is important to note that the minus sign of amplitude does not necessarily mean that the waves are antiphase with the original disturbance, because there is another determinant factor, the coupling factor M_3, whose the sign may change from case to case, depending on the vertical stratification of the study area. If the coupling factor M_3 is negative (positive), the SAR imagery will be inphase (antiphase) with the topographic waves. All other factors have no influence on the sign, because they always take positive values. Furthermore, the radar signals would significantly be strengthened, if one of upper layer resonance conditions (31) and (33) is met.

4.5. Solutions for Two and One Layer Oceans

[36] In the above derivation and analysis, a three layer ocean model was considered, but there were not any beforehand restraints for the thickness of any layers. Therefore the solutions for a two layer ocean can be obtained by setting H = 0 in (21) and (22)

$$W_1(x,z) = (W_s/\pi M_0)[\sin n_1 z + M_0 \cos n_1 z]e^{ikx}, \tag{44}$$

and

$$W_2(x,z) = (W_s/\pi M_0)[\sin n_1(2\Delta H) + M_0 \cos n_1(2\Delta H)] \bullet \cdot \exp[-\gamma_2\{z - 2\Delta H\} + ikx]. \tag{45}$$

Similarly to the three-layer model ocean, we have a frequency relation $N_2 < \sigma < N_1$. Accordingly, the SAR image of bottom topographic waves becomes

$$\sigma_\circ|_{os} = -\left[16\pi k_0^4 |g_{ij}(\theta)|^2\right] \bullet \left[\frac{\cos^2\phi}{2m_3\omega K^4}\right] \bullet \left[\frac{n_p W_s}{\pi} M_2 e^{-n_p H_2}\right] \cos kx, \tag{46}$$

where $n_2 = in_p$, and subscript 2 represents the upper layer of the ocean instead of 3.

[37] The solutions for a one layer ocean can be obtained by setting $H = \Delta H = 0$ in (22)

$$W(x,z) = (W_s/\pi)\exp i(nz + kx). \tag{47}$$

The frequency relation is $N < \sigma$. The SAR image of bottom topographic waves becomes

$$\sigma_\circ|_{os} = -\left[16\pi k_0^4 |g_{ij}(\theta)|^2\right] \bullet \left[\frac{\cos^2\phi}{2m_3\omega K^4}\right] \bullet \left[\frac{n_p W_s}{\pi} e^{-n_p D}\right] \cos kx. \tag{48}$$

5. Comparison With Observations

[38] The above hydrodynamic analyses reveal the following dynamical features of ocean bottom topographic waves for a three layer ocean. (1) In the lower layer, the ocean bottom topographic waves are generated by bottom topographic corrugation. The waves exist in the form of station-

Table 3. Stratification Parameters at the CTD Stations

Station	Depth, m	CTD Depth, m	H_3, m	$2\Delta H$, m	H_1, m	σ, cph	N_3, cph	N_2, cph	N_1, cph
C044S01	81	73	20	40	21	6.5	6	15	3
C044S02	63	54	5	40	9	6.5	6	20	3
C044S03	37	27	7	13	17	6.5	6	35	3
C044S04	25	15	25	0	0	6.5	5	-	-
C044S05	26	20	26	0	0	6.5	4	-	-
C044S06	31	28	31	0	0	6.5	3	-	-
Y90	56	53	5	30	21	6.5	4	22	3
Y92	92	71	40	30	22	6.5	4	22	N/A
Y94	140	138	24	60	56	6.5	4	15	5
Y96	450	300	40	80	330	_	5	15	5
Y98	1709	570	30	160	1579	_	5	12	5

ary waves, which satisfy a lower boundary resonance condition $\sigma = kC_0$, in which k is a wave number of bottom topographic corrugation, and C_0 is a background current speed. (2) The bottom topographic waves may vertically propagate to the upper layer with an unchanged wave number k, if a frequency relation $N_3 < \sigma < N_2$ is satisfied. (3) The waves are extremely amplified if a upper layer resonance condition is satisfied. (4) The topographic waves on SAR images have the same wavelength of bottom topographic corrugation, and the imagery brightness peaks are either inphase (phase shift 0) or antiphase (phase shift π) with respect to the topographic waves, depending on signs of the coupling factor. From the solutions of three layer ocean, it is easy to derive the solutions for two or one layer ocean. In this section, we will verify these major dynamical features using field observations and satellite remote sensing data.

5.1. Stationary Waves and Wavelength

[39] Theoretical model predicts that the topographic waves are stationary waves, if the lower layer resonance condition (20), $\sigma = kC_0$, is satisfied. This prediction can be verified by multiple SAR images of topographic waves in Taiwan Banks within three years from 1994 to 1996 (940727, 950603, 950622, and 960619). Comparisons between these images reveal only a little change in the locations, patterns, and distribution extent of the topographic waves. *Li et al.* [2001] compared the SAR imagery of the topographic waves with LANDSAT TM visible band imagery taken at a different time and found a very good correspondence between the two. These facts indicate that the observed topographic waves are not only stationary waves, but also in a quite stable condition.

[40] The analytical expression of SAR image of bottom topographic waves (43) predicts that the SAR imagery of bottom topographic waves should appear as the form of sinusoidal function with the same wave number of original bottom topographic waves. The depth profile measured by the on-board ADCP and collocated radar imagery brightness curve shown in Figure 4 show that fluctuations in the bottom topography and radar return are composed of multifrequency/wave number components. Here we do not intend to determine the exact correspondence between the pulses in the two curves because of the limited resolution of the SAR image (100 m). But, the data may still be used to verify the theoretical solution (43). Instead of one by one comparison, a spectral or statistical analysis method is used for the verification. The Fourier spectra derived from high-pass filtered data are shown in Figure 9. One can see that the two spectra have almost the same shape with an identical peak location at 1.2 km^{-1}, which is corresponding to 0.83 km, a dominant or peak-power wavelength of topographic waves along the ADCP track. Thus the theoretical prediction of an identical wavelength on the SAR images is verified.

5.2. Hydrodynamic Conditions for the Topographic Waves

[41] In section 4.3, we derived the frequency relation for the generation and vertical propagation of topographic waves in the stratified model ocean (25). In our case, the dominant or peak-power wavelength of topographic waves is 0.83 km, and the tidal speed is 1.5 ms^{-1}. Thus, from the lower layer resonance condition (20), we derive the angular frequency of topographic waves σ = 6.5 cph (cycle per hour). Meanwhile, from section 2.4 and Figure 2, we derive the average Brunt-Wäisälä frequencies of each layer at the CTD stations as listed in Table 3. One can see that the frequency relation $N_3 < \sigma < N_2$ is satisfied for three layer oceans at Stations C044S01- 03 and Y90 – 98, and $N < \sigma$ for one layer ocean at Stations C044S04 - 06.

5.3. Spatial Phase of SAR Imagery and Radar Signal Enhancement

[42] From the solution of bottom topographic wave SAR imagery (43) for three layer ocean, one can see that the spatial phase of SAR imagery with respect to the bottom topographic waves depends on the sign of the coupling factor M_3 in the form of (28). The SAR imagery should be inphase (antiphase) with the topographic waves, if M_3 takes a minus (plus) sign. On the other hand, the sign of M_3 depends on Θ and μ. Using definitions (10), (23), (28), and field data listed in Table 3, we calculate these parameters at the CTD stations. The results are listed in Table 4. One can see two important points. (1) In all the cases, M_3 takes the minus sign, implying that the SAR imagery is inphase with the bottom topographic waves. (2) At Station Y98, the radar return signals are enhanced by near satisfaction of the upper layer resonance conditions. Unfortunately, that station is beyond SAR image coverage.

[43] On the other hand, examining imagery patterns on the SAR image, one can see that the wave-like patterns consist of two subsystems with different scales and orientations. One subsystem has a wavelength scale on the order of 5 km, lengths ranging from 20 to 40 km, and a north-south (or top-bottom on the image) orientation. In comparison to the field observations, we interpret them as imagery of submarine sand ridges. The other subsystem riding on the large scale system has a wavelength scale

Table 4. Vertical Wave Numbers and Coupling Parameters Between Upper Two Layers at CTD Stations

Station	n_2, k	n_p, k	μ	Θ, π	M_3
C044S01	2.1	0.38	0.18	0.20	1.1
C044S02	2.9	0.38	0.13	0.28	1.4
C044S03	5.3	0.38	0.072	0.17	1.1
Y90	3.2	0.79	0.25	0.23	1.1
Y92	3.2	0.79	0.25	0.23	1.1
Y94	2.1	0.79	0.38	0.30	1.1
Y96	2.1	0.64	0.30	0.40	1.7
Y98	1.6	0.64	0.40	0.62	256

on the order of 1 km, and takes a west-east (or left-right on the image) orientation. They occupy two thirds of the bright area. From the spectra shown in Figure 9, we obtain the peak-power wavelength as 0.83 km, which is comparable with previous results [*Hsu et al.*, 1997; *Li et al.*, 2001; *Alpers et al.*, 2004]. The imagery features, including distribution patterns, scales, orientations, in particular narrow separations and wide widths of grouped sand waves, indicate that the bright imagery bands correspond to the troughs of bottom topographic waves. This agrees with theoretical prediction.

[44] Moreover, the CTD data shown in Figures 2a and 2b indicate that the vertical stratifacation of the shallow water region, represented by Stations C044S04 - 06 and mainly distributed in the north study area, can be described well by a one layer ocean model with weakly continuous stratification. The solution of one layer ocean indicates that the imagery brightness peaks are also antiphase (phase shift π) with respect to the topographic waves. This phase shift of π is close to that observed by *Donato et al.* [1997] on the continental shelf east of Cape Hatteras.

6. Conclusions

[45] The goal of this investigation is to explore satellite SAR imaging mechanisms of ocean bottom topographic features for a stratified ocean. The results are used for a quantitative interpretation of SAR images of bottom topographic waves. The Taiwan Banks area located at the south outlet of Taiwan Strait is selected as a study area, where the bottom features at depths up to 100 m show up on the SAR images with very high imagery contrast, and where simultaneous or quasi-simultaneous cruise data are available. On the basis of hydrographic conditions and the bottom features in the study area, a two-dimensional, three-layer ocean model with sinusoidal bottom topographic corrugation is developed. From the solutions and inferences derived from the momentum equations of the ocean model and verified by observations, the following major conclusions are drawn.

[46] 1. Under the conditions of the existence of a crossing current and the smallness of the amplitude of bottom topographic corrugation compared to the water depth, the topography serves as a source of disturbance to induce stationary water waves in the lower layer. The waves satisfy the lower boundary resonance condition $\sigma = kC_0$, here σ is the angular frequency of the stationary water waves, k is the wave number of the sinusoidal bottom topographic corrugation, and C_0 is the crossing current speed.

[47] 2. The bottom topographic waves are internal waves. The waves may propagate vertically to the upper layer with the same wave number, under the condition of that the frequency relations $N_j < \sigma < N_i$ are satisfied for three and two layer oceans, here N_i and N_j (i = 1, 2, and j = 2, 3) are the Brunt-Wäisälä frequencies of middle (lower) layer and upper layer, and $N < \sigma$ for a one layer ocean, respectively. Physically, this relation requires that the water density has a sharp increase in the middle (lower) layer for the three (two) layer ocean. CTD measurements at all stations within the study area indicate that the relation holds stood in the SAR imaging season.

[48] 3. The amplitude of topographic waves in the upper layer depends on the coupling factor $M_3 = n_2[n_2 \cos n_2(2\Delta H) + n_p \sin n_2(2\Delta H)]^{-1}$ (see text for parameter definitions) for the three layer ocean. This implies that there is a resonance mechanism, i.e., M_3 may reach a quite large number when the term in the square bracket takes a number much smaller than n_2. In this case, the radar return signals are extremely amplified.

[49] 4. The physical expression of SAR image of topographic waves is derived on the basis of current-modulated small wave spectra developed by *Yuan* [1997]. The expression indicates that the topographic waves on SAR image should have the same wave patterns with the same wavelength of bottom topographic corrugation. The imagery brightness peaks are either inphase or antiphase with respect to the topographic corrugation, depending on the sign of coupling factor M_3. In the case of SAR image 940727, M_3 is always a positive number, so that the bright imagery bands correspond to the troughs of bottom topographic waves.

[50] **Acknowledgments.** The authors would like to express their thanks to Jianyu Hu for providing current measurements and to Shoujing Wang for computing the tidal current vectors. This work was supported by ONR through grants N00014-05-1-0328 and N00014-05-1-0606 (for Q. Zheng); by MST, China through grants KISTCP 2002CB714001 (for L. Li) and NBRPC G1999043805 (for X. Guo and Y. Ge); and by NSFC, China through grant 40476023 (for D. Zhu).

References

Alpers, W., and I. Hennings (1984), A theory of the imaging mechanism of underwater bottom topography by real and synthetic aperture radar, *J.Geophys.Res.*, *89*, 10,529–10,546.

Alpers, W., G. Campbell, H. Wensink, and Q. Zheng (2004), Underwater topography, in *Synthetic Aperture Radar Marine User's Manual*, edited by C. Jackson and J. Apel, pp. 245–262, Natl. Environ. Satell., Data, and Inf. Serv., Natl. Oceanic and Atmos. Admin., Silver Spring, Md.

Apel, J. R. (1987), *Principles of Ocean Physics*, Elsevier, New York.

Cai, A., X. Zhu, Y. Li, and Y. Cai (1992), Sedimentary environment in Taiwan Shoal, *Chin. J. Oceanol. Limnol.*, *10*, 331–339.

Chen, Z., J. Hu, C. Zhang, X. Zhang, F. Lin, H. Liang, and J. Hong (1999), The characteristics of tidal current and residual current in the southern Taiwan Strait in August, 1997, *J. Xiamen Univ. Natl.*, 268–272.

Chuang, W. S. (1986), A note on the driving mechanism of the current in the Taiwan Strait, *J. Oceanogr. Soc. Jpn*, *42*, 355–361.

Donato, T. F., F. Askari, G. O. Marmorino, C. L. Trump, and D. R. Lyzenga (1997), Radar imaging of sand waves on the continental shelf east of Cape Hatteras, NC, U.S.A., *Cont. Shelf Res.*, *17*, 989–1004.

Fu, L.-L., and B. Holt (1982), Seasat views oceans and sea ice with synthetic aperture Radar, *JPL Publ.*, *81-120*.

Gossard, E. E., and W. H. Hooke (1975), *Waves in the Atmosphere*, Elsevier, New York.

Gossard, E. E., and W. H. Munk (1954), On gravity waves in the atmosphere, *J. Meteorol.*, *11*, 259–269.

Guan, B., and G. Fang (2006), Winter counter-wind currents off the southeastern China coast: A review, *J. Oceanogr.*, *62*, 1–24.

Hennings, I. (1990), Radar imaging of submarine sand waves in tidal channels, *J. Geophys. Res.*, *95*, 9713–9721.

Hsu, M.-K., L. M. Mitnik, and S.-M. Shih (1997), Mapping of sand waves and channels in the Taiwan Tan area with ERS SAR, paper presented at 3rd ERS Symposium on Space at the Service of Our Environment, Eur. Space Agency, Florence, Italy, 17–21 March.

Jan, S., C.-S. Chern, J. Wang, and S.-Y. Chao (2004), The anomalous amplification of M2 tide in the Taiwan Strait, *Geophys. Res. Lett.*, *31*, L07308, doi:10.1029/2003GL019373.

Klein, L. A., and C. T. Swift (1977), An improved model for the dielectric constant of sea water at microwave frequencies, *IEEE Trans. Antennas Propag.*, *AP-25*, 104–111.

Kuo, N.-J., and C.-R. Ho (2004), ENSO effect on the sea surface wind and sea surface temperature in the Taiwan Strait, *Geophys. Res. Lett.*, *31*, L13309, doi:10.1029/2004GL020303.

Li, L., and D. Li (1989), Summer hydrographic features of channel west of Taiwan Shoals and the coastal upwelling, *J. Oceanogr. Taiwan Strait*, *8*, 353–359.

Li, L., W. D. Nowlin Jr., and J. Su (1998), Anticyclonic rings from Kuroshio in the South China Sea, *Deep Sea Res., Part I*, *45*, 1469–1482.

Li, L., X. Guo, and R. Wu (2000), Oceanic fronts in southern Taiwan Strait, *J. Oceanogr. Taiwan Strait*, *19*, 147–156.

Li, Y., L. Ma, J. Yang, and A. Shi (2001), Study on stability of sand waves by satellite sensing, in *The Proceedings of the First Asian and Pacific Coastal Engineering Conference, APACE 2001, Dalian, China*, edited by D. Qiu and Y. Li, pp. 850–856, Dalian Univ. of Technol. Press, Dalian, China.

Li, Y., J. Hu, J. Li, B. Fu, and L. Ma (2003), Optical image modulation above the submarine bottom topography: A case study on the Taiwan Banks, China, in *Ocean Remote Sensing and Applications*, edited by R. J. Frouin, Y. Yuan, and H. Kanamura, *Proc. SPIE Int. Soc. Opt. Eng.*, *4892*, 382–390.

Lodge, D. W. (1983), Surface expressions of bathymetry on SEASAT synthetic aperture radar images, *Int. J. Remote Sens.*, *4*, 639–653.

Plant, W. J. (1990), Bragg scattering of electromagnetic waves from the air/sea interface, in *Surface Waves and Fluxes*, vol. 2, *Remote Sensing*, edited by G. L. Geernaert and W. J. Plant, pp. 41–108, Springer, New York.

Saxton, J. A., and J. A. Lane (1952), Electrical properties of sea water, *Wireless Eng.*, *291*, 269–275.

Shuchman, R. A., D. R. Lyzenga, and G. A. Meadows (1985), Synthetic aperture radar imaging of ocean-bottom topography via tidal-current interactions: Theory and observations, *Int. J. Remote Sens.*, *6*, 1179–1200.

van der Kooij, M. W. A., J. Vogelzang, and C. J. Calkoen (1995), A simple analytical model for brightness modulations caused by submarine sand waves in radar imagery, *J. Geophys. Res.*, *100*, 7069–7082.

Vogelzang, J. (1989), The mapping of bottom topography with imaging radar: A comparison of the hydrodynamic modulation in some existing models, *Int. J. Remote Sens.*, *10*, 1503–1518.

Vogelzang, J. (1997), Mapping submarine sand waves with multiband imaging radar: 1. Model development and sensitivity analysis, *J. Geophys. Res.*, *102*, 1163–1181.

Yin, F. (1984), Tides around Taiwan, in *Ocean Hydrodynamics of the Japan and East China Seas*, edited by T. Ichiye, pp. 301–315, Elsevier, New York.

Yuan, Y. (1997), Representation of high frequency spectra of ocean waves and the basis for analyzing SAR images, *Chin. J. Oceanol. Limnol.*, *28*, 1–5.

Zheng, Q., and V. Klemas (1982), Determination of winter temperature patterns, fronts, surface currents in the Yellow Sea and East China Sea from satellite imagery, *Remote Sens. Environ.*, *12*, 201–218.

Zheng, Q., X.-H. Yan, V. Klemas, C.-R. Ho, N.-J. Kuo, and Z. Wang (1998), Coastal lee waves on ERS-1 SAR images, *J. Geophys. Res.*, *103*, 7979–7993.

Zheng, Q., Y. Yuan, V. Klemas, and X.-H. Yan (2001), Theoretical expression for an ocean internal soliton SAR image and determination of the soliton characteristic half width, *J. Geophys. Res.*, *106*, 31,415–31,423.

Zheng, Q., P. Clemente-Colón, X.-H. Yan, W. Timothy Liu, and N. E. Huang (2004), Satellite SAR detection of Delaware Bay plumes: Jet-like feature analysis, *J. Geophys. Res.*, *109*, C03031, doi:10.1029/2003JC002100.

Y. Ge, X. Guo, and L. Li, Third Institute of Oceanography, State Oceanic Administration, 361006 Xiamen, China.

C. Li, Coastal Studies Institute, Department of Oceanography and Coastal Sciences, Louisiana State University, Baton Rouge, LA 70803, USA.

Q. Zheng, Department of Atmospheric and Oceanic Science, University of Maryland, College Park, MD 20742-2425, USA. (quanan@atmos.umd.edu)

D. Zhu, Department of Oceanography, Xiamen University, 361005 Xiamen, China.